M1 and E2 transition rates from core-excited states in semi-magic ^{94}Ru

A. Ertoprak[1,2,a], B. Cederwall[1], C. Qi[1], M. Doncel[1,3], U. Jakobsson[1,4], B. M. Nyakó[5], G. Jaworski[6], P. Davies[7], G. de France[8], I. Kuti[5], D. R. Napoli[6], R. Wadsworth[7], S. S. Ghugre[9], R. Raut[9], B. Akkus[2], H. Al Azri[7], A. Algora[5,10], G. de Angelis[6], A. Atac[1], T. Bäck[1], A. Boso[11], E. Clément[8], D. M. Debenham[7], Zs. Dombrádi[5], S. Ertürk[12], A. Gadea[10], F. Ghazi Moradi[1], A. Gottardo[13], T. Hüyük[10], E. Ideguchi[14], H. Li[1], C. Michelagnoli[8], V. Modamio[6], J. Nyberg[15], M. Palacz[16], C. M. Petrache[13], F. Recchia[11], M. Sandzelius[17], M. Siciliano[6], J. Timár[5], J.J. Valiente-Dobón[6] and Z. G. Xiao[18a]

1. Department of Physics, Royal Institute of Technology (KTH), SE-10691 Stockholm, Sweden
2. Department of Physics, Faculty of Science, Istanbul University, Vezneciler/Fatih, 34134, Istanbul, Turkey
3. Department of Physics, Oliver Lodge Laboratory, University of Liverpool Liverpool L69 7ZE
4. United Kingdom Department of Chemistry, P.O. Box 3, 00014 University of Helsinki, Finland
5. MTA Atomki, H-4001 Debrecen, Hungary
6. Istituto Nazionale di Fisica Nucleare, Laboratori Nazionali di Legnaro, I-35020 Legnaro, Italy
7. Department of Physics, University of York, Heslington, York, YO10 5DD, United Kingdom
8. Grand Accélérateur National d'Ions Lourds (GANIL), CEA/DSM - CNRS/IN2P3, Bd Henri Becquerel, BP 55027, F-14076 Caen Cedex 5, France
9. UGC-DAE Consortium for Scientific Research, Kolkata Centre, Kolkata 700098, India
10. Instituto de Física Corpuscular, CSIC-Universidad de Valencia, E-46980 Valencia, Spain
11. Dipartimento di Fisica e Astronomia, Università di Padova, Padova, Italy
12. Nigde Omer Halisdemir University, Science and Art Faculty, Department of Physics 51200 Nigde, Turkey
13. Centre de Sciences Nucléaires et Sciences de la Matière, CNRS/IN2P3, Université Paris-Saclay, 91405 Orsay, France
14. Research Center for Nuclear Physics, Osaka University, Osaka, Japan
15. Department of Physics and Astronomy, Uppsala University, SE-75120 Uppsala, Sweden
16. Heavy Ion Laboratory, University of Warsaw, Pasteura 5A, PL 02-093, Warsaw, Poland
17. University of Jyväskylä, Department of Physics, FI-40014, Jyväskylä, Finland
18. Department of Physics, Tsinghua University, Beijing 100084, China

Abstract. Lifetimes of high-spin states have been measured in the semi-magic (N=50) nucleus ^{94}Ru. Excited states in ^{94}Ru were populated in the ^{58}Ni(^{40}Ca, $4p$)^{94}Ru* fusion-evaporation reaction at the Grand Accélérateur National d'Ions Lourds (GANIL) accelerator complex. DSAM lifetime analysis was performed on the Doppler broadened line shapes in energy spectra obtained from γ-rays emitted while the residual nuclei were slowing down in a thick 6 mg/cm^2 metallic ^{58}Ni target. In total eight excited-state lifetimes in the angular momentum range $I = (13 - 20)\hbar$ have been measured, five of which were determined for the first time. The corresponding B(M1) and B(E2) reduced transition strengths are discussed within the framework of large-scale shell model calculations to study the contribution of different particle-hole configurations, in particular for analyzing contributions from core-excited configurations.

PACS. PACS-key discribing text of that key – PACS-key discribing text of that key

1 Introduction

The level structure of ^{94}Ru and other semi-magic nuclei with neutron or proton numbers equal to 50 are of special importance for testing state-of-the-art theory, in particular within the configuration interaction ("shell model") framework. The main structural features of low-lying states in nuclei just below the $N = Z = 50$ shell closures can

within this framework be well described by the relatively isolated $0g_{9/2}$ and $1p_{1/2}$ subshells. Of particular interest is the competition between the neutron-proton pair coupling scheme that is expected to dominate in the $N = Z$ nuclei (see Refs. [1,2] and Refs. therein) and the "normal" seniority structure of the $N = 50$ isotones. For example, the low-lying yrast states of ^{96}Pd and ^{94}Ru show similar yrast structures, reflecting an approximate conservation of seniority symmetry up to seniority $\nu = 4$.

a *e-mail: ertoprak@kth.se*

More "realistic" descriptions of the structures of these nuclei may be obtained through large-scale shell-model (LSSM) calculations by including the neighboring $1p_{3/2}$ and $0f_{5/2}$ orbitals [3], as well as core-excited configurations involving the excitation of nucleons across the $N = Z = 50$ shell gap [4]. Lifetime measurements provide powerful tools to test such model descriptions, going significantly beyond the constraints made by energy level measurements. In particular, the reduced magnetic dipole and electric quadrupole transition probabilities, B(M1) and B(E2), respectively, directly probe the nuclear wave functions. In this work, such measurements are employed in order to probe the structure of intermediate to high-spin states in ^{94}Ru where core-excited states, based on neutron excitations across $N = 50$ shell closure, are expected to play a key role.

2 Experimental Set-up

High-spin states in ^{94}Ru have been populated via the ^{58}Ni(^{40}Ca, $4p$)^{94}Ru* fusion-evaporation reaction at the Grand Accélérateur National d'Ions Lourds (GANIL), Caen, France. The ^{40}Ca ions were accelerated to an energy of 150 MeV, degraded to 128 MeV in a thin Ta foil, and used to bombard target foils consisting of 99.9% isotopically enriched ^{58}Ni with areal density of 6 mg/cm^2, which is sufficient to stop the fusion products of interest. The beam intensity varied between 5 - 10 pnA with and average of 7 pnA during 14 days of irradiation time. Prompt γ-rays emitted in the reactions were detected by the EXOGAM spectrometer array [5], consisting of 11 Compton-suppressed segmented HPGe clover detectors placed in two rings, at angles 90° and 135° relative to the direction of the beam. EXOGAM was used in a close-packed configuration with the front part of each BGO Compton suppression shield removed from the clover detectors. Emission of light charged particles and neutrons was detected in prompt coincidence with the γ-rays by the nearly 4π solid angle charged particle detector array DIAMANT [6, 7], consisting of 80 CsI(Tl) scintillators and the Neutron Wall [8], an array of 50 organic liquid-scintillator detectors covering a 1π solid angle in the forward direction. The Neutron Wall detection efficiency is typically 25% while the proton- and α-particle efficiencies are around 55% and 48%, respectively. The hardware trigger condition for recording events for subsequent off-line analysis was one escape-suppressed γ-ray registered in any of the Ge clover detectors and one neutron-like event detected in the Neutron Wall. The condition for the neutron-like events was determined by a hardware threshold on the zero-crossing time of the signals from the Neutron Wall shaping amplifiers and was sufficiently relaxed to allow also a sizeable fraction of γ-ray induced signals. As a result, the majority of the events collected were due to the most prolific pure charged particle evaporation reactions, such as the ^{58}Ni(^{40}Ca, $4p$)^{94}Ru* reaction studied in the present work. In addition, no charged-particle selection was needed for the γ-ray energy spectra used in the DSAM analysis of excited states in ^{94}Ru. The final discrimination between neu-

trons and γ-rays in Neutron Wall was performed off-line by setting two-dimensional gates on the neutron time-of-flight versus the zero-cross-over time in the shaping amplifiers. For the off-line charged particle selection, individual two-dimensional gates on the "particle identification" and "energy" parameters of the DIAMANT detectors enabled the identification of γ-rays as belonging to specific charged particle evaporation channels. A 50 ns wide time gate was applied to the time-aligned Ge detector timing signals in order to select prompt γ-ray emission. The energy calibration of the germanium detectors was performed using standard radioactive sources (^{60}Co and ^{152}Eu). Lifetimes of excited states in ^{94}Ru were deduced from an analysis of the Doppler broadened line shapes resulting from the emission of the γ-rays while the residual nuclei were slowing down in the thick (6 mg/cm^2) metallic ^{58}Ni target.

3 Data Analysis and Results

The off-line analysis of selected γ-ray coincidence matrices and spectra was performed using the RADWARE software package [9]. The observation of Doppler-broadened line shapes enabled the determination of level lifetimes using the Doppler Shift Attenuation Method (DSAM) [10]. In standard DSAM measurements a thin target coupled with a thick backing material normally ensures that the production cross section for the fusion-evaporation residues can be assumed to be constant across the target. Here, the use of a thick homogeneous production target resulted in a substantial decrease in the energy of the incident projectiles as they traversed the target with an associated change in the production cross section of the residues as a function of penetration depth. However, since the kinetic energy of the ^{40}Ca ions incident on the target, 128 MeV, is close to the Coulomb barrier, the majority of the fusion reactions were induced by the beam particles in only the first thin (~ 1 mg/cm^2) layer of the target. The cross section for production of the ^{94}Ru residues varied strongly in this layer and the remaining part of the target thickness acted merely as a stopping medium, i.e. corresponding to the "backing" used in conventional DSAM measurements. The residue production rate as a function of target depth and the associated effective target thickness follows from the information on the reaction cross-section dependence on the beam energy and the evolution of the latter along the target thickness. The cross section for the production of the fusion residues as a function of beam energy can be obtained from experimental data and/or from statistical model calculations using, e.g., the PACE4 code [11] with varying accuracy. Here, due to the strong variation of the fusion cross section as a function of beam particle kinetic energy close to the Coulomb barrier, the DSAM analysis is particularly challenging and we rely on the detailed experimental cross section data obtained by Bourgin *et al.* [12]. The stopping powers used in the analysis were calculated using the SRIM software package [13,14]. Doppler broadening lineshapes in the energy spectra due to γ-rays emitted from short lived states while the fusion products were slowing down in the target were observed.

As an example, Doppler broadening in the lineshapes of the 630 keV ($17_1^+ \rightarrow 16_1^+$) and 543 keV ($14_1^+ \rightarrow 13_1^+$) transitions in ^{94}Ru are clearly visible in the spectra gated on the moving components of the direct feeding transitions, see Fig. 1.

The program LINESHAPE [15] in a modified version, see Ref. [16], was used to calculate the expected Doppler shape for a given γ-ray transition at a particular detector angle and perform a least-square fit to the corresponding experimental spectrum in order to extract the level lifetime (τ). Intrinsic lineshape effects due to, e.g., neutron-induced defects in the germanium crystals were taken into account in the fitting function. The intrinsic asymmetry of the peak shapes was determined from a systematic study of transitions for which the residual nuclei were completely stopped and fitted to a superposition of Gaussian functions given by

$$f(e) = N \cdot \frac{1}{\sigma\sqrt{2\pi}}(e^{-(e-c)^2/2\sigma^2} + a \cdot e^{-(e-c-k\cdot2\sqrt{2ln2}\sigma)^2/2\sigma^2})$$
(1)

where N is a normalization factor proportional to the total peak area (i.e. intensity), c is the centroid of the symmetric Gaussian component, k = 1.29 and a = 0.07 are constants obtained from the fits, and σ is an energy dependent width determined by fitting the full-width-at-half-maximum, $FWHM = 2\sqrt{2ln2}\sigma$ to several known stopped

Table 1. Relative γ-ray intensities for ^{94}Ru measured in the present work.

Positive Parity			Negative Parity		
$I_i^\pi \rightarrow I_f^\pi$	E_γ (keV)	I_γ	$I_i^\pi \rightarrow I_f^\pi$	E_γ (keV)	I_γ
$14_1^+ \rightarrow 13_1^+$	543.4	45.3(9)	$18_1^- \rightarrow 16_1^-$	932	4.8(3)
$15_1^+ \rightarrow 14_1^+$	615.6	28.2(7)	$20_1^- \rightarrow 18_1^-$	1113.5	6.1(2)
$16_1^+ \rightarrow 15_1^+$	638.5	17.7(4)	$17_2^- \rightarrow 15_2^-$	1288	0.0030(7)
$17_1^+ \rightarrow 16_1^+$	630.1	21.7(5)	$15_2^- \rightarrow 14_1^+$	1344	4.5(2)
$18_1^+ \rightarrow 17_1^+$	486.0	13.6(4)	$15_2^- \rightarrow 14_2^+$	462	1.1(3)
$19_1^+ \rightarrow 18_1^+$	394.5	9.9(3)	$15_3^- \rightarrow 15_1^+$	964	0.98(8)
$15_1^+ \rightarrow 13_1^+$	1159	4.0(1)	$16_2^- \rightarrow 15_2^-$	1225	0.8(1)
$16_1^+ \rightarrow 14_1^+$	1254	1.4(1)	$18_1^- \rightarrow 18_1^+$	402	< 0.001
$15_2^+ \rightarrow 13_1^+$	1296	3.4(1)	$16_3^- \rightarrow 15_2^-$	610.6	0.028(4)
$17_1^+ \rightarrow 15_1^+$	1269	1.5(1)	$17_1^- \rightarrow 16_1^-$	257.3	11.7(6)
$18_1^+ \rightarrow 16_1^+$	1115	0.02	$17_2^- \rightarrow 16_1^-$	792.4	4.1(2)
$19_1^+ \rightarrow 17_1^+$	880	2.3(1)	$17_2^- \rightarrow 16_3^-$	325	0.012(1)
$15_2^+ \rightarrow 14_1^+$	753	9.2(3)	$19_1^- \rightarrow 17_1^-$	1190.4	0.029(2)
$16_1^+ \rightarrow 14_1^+$	501	6.4(2)	$20_1^- \rightarrow 19_1^-$	597.5	1.39(9)
$10_1^+ \rightarrow 8_1^+$	1347	100	$16_2^- \rightarrow 15_3^-$	398.1	1.6(1)
			$16_1^- \rightarrow 15_2^-$	496	21.9(8)
			$16_2^- \rightarrow 15_4^-$	281.6	1.1(1)
			$17_2^- \rightarrow 16_2^-$	654	0.80(7)
			$18_1^- \rightarrow 17_1^-$	674	1.7(1)
			$18_2^- \rightarrow 18_1^-$	616.4	0.085(8)
			$19_1^- \rightarrow 18_1^-$	515.6	3.2(3)

peaks using the function $FWHM(e) = \sqrt{A + B \cdot e + C \cdot e^2}$ in the standard RADWARE fashion [9]. This is illustrated in Fig. 2.

Due to the intrinsic lineshape effects discussed above, it was not possible to avoid that some fraction of the fully stopped component was included in such gates, since the Doppler-shifted component of the peaks overlay with the left-side tail of the intrinsic lineshape due to charge trapping in the Ge crystals. Therefore, lifetimes in ^{94}Ru were analyzed using the Narrow Gate on Transition Below (NGTB) method [10].
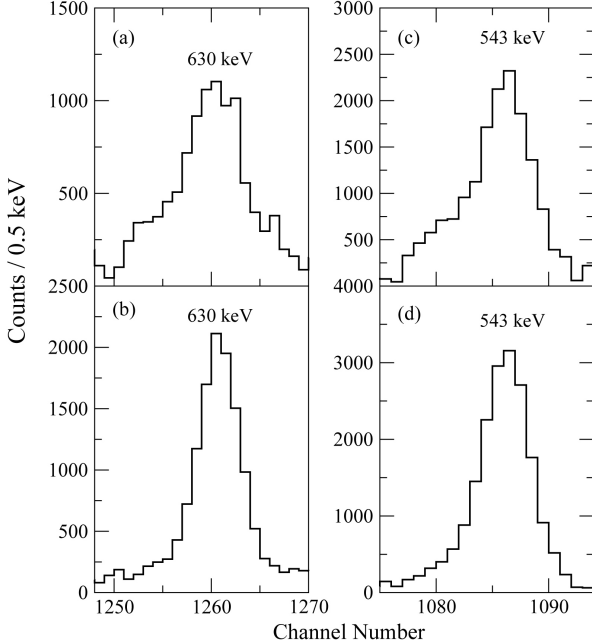

Fig. 1. Experimental γ-ray energy spectra for the 630 keV ($17_1^+ \rightarrow 16_1^+$) and 543 keV ($14_1^+ \rightarrow 13_1^+$) transitions generated by gates on the direct feeding transitions in the level scheme. The top panels (a,c) show spectra produced by gating on the Doppler-shifted components (left side) of the asymmetric peaks, exhibiting clearly Doppler-broadened lineshapes. For the spectra in the lower panels (b,d), which were produced by gating on the stopped components of the peaks, no Doppler broadening is visible. See text for details.
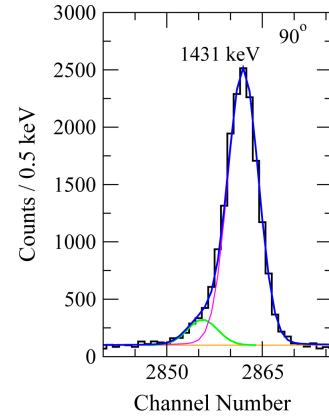

Fig. 2. (Color online) Experimental γ-ray energy spectrum for the completely stopped 1431 keV ($2_1^+ \rightarrow 0_1^+$) transition in ^{94}Ru observed at $90°$ with respect to the beam direction. The decomposition of the intrinsic lineshape into two Gaussian peaks and their sum (magenta, green, and blue, respectively) used for the lineshape analysis in this work is also shown. The spectrum was produced by requiring prompt coincidences with the 439 keV transition decaying from the 5_1^- state at 2624 keV excitation energy. See text for details.

The procedure in which a gate on a lower transition with respect to the transition of interest is made, developed by Brandolini and Ribas for the analysis of DSAM measurements [10]. Therefore, the side feeding coming from higher-lying excited states has been taken into account for the lifetime determination. For this purpose, branching ratios for the γ-decays into and out of the states of interest were studied in detail in the present work, see Table 1 and Fig. 3. In the present case the analysis is facilitated by the fact that several lifetimes in ^{94}Ru for the relevant spin range have been determined previously using the recoil distance Doppler shift technique [18] as discussed further below.
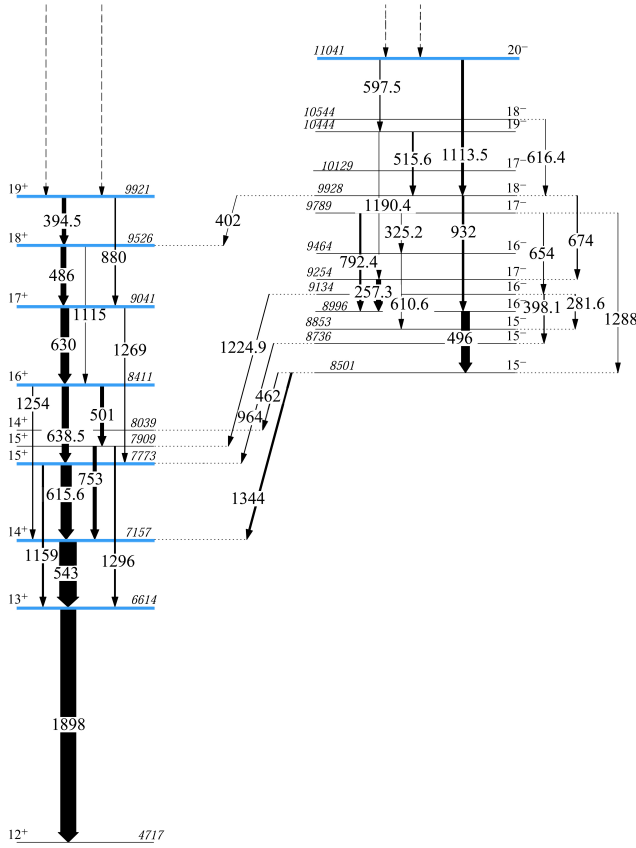

Fig. 3. (Color online) Partial level scheme of ^{94}Ru. Spins and parities are taken from the work of Ghazi-Moradi *et al.* Ref. [20]. The lifetimes of the levels which are highlighted in blue have been measured in the present work.

The method used in this work has previously been validated using the lifetime of the $I^\pi = 18^+$ state in the ^{94}Ru nucleus [17] by comparing with the value obtained in a previous measurement [18] using a different (RDDS) technique.

Due to the low energy employed for the reaction, many of the states of interest receive significant amounts of direct feeding. For example, for the highest-lying states considered here; the 19^+ excited state at 9921 keV and the 20^- excited state at 11041 keV, the feeding transitions

that have previously been observed from states that are situated at 1.9 - 3.8 MeV higher excitation energy [19], were not observed in the present experiment, presumably due to the significantly lower excitation energy in the present reaction. It is therefore reasonable to assume that the 19^+ and 20^- states receive direct, very fast feeding. This conclusion is supported by the fact that the previously known lifetimes of states measured by Jungclaus et al. [18], which lie below the 19^+ and 20^- states, are well reproduced in the present analysis with this assumption. For the yrast positive-parity states in the spin range $I = (13 - 18)\hbar$ analyzed in this work, the Bateman equations, where the side feeding is included, have been applied. In addition, an iterative process has been performed in such a way that once the lifetime of a certain state has been determined it has been used as an input value for the next lower level in the γ-ray cascade, and so on. Intermediate verifications could be obtained due to the known values for the lifetimes of the 18^+ and 14^+ excited states, measured by Jungclaus et al. [18]. As can be seen in Table 2, also the limits established for the 15^+, 16^+, and 17^+ excited states in Ref. [18] are in agreement with the values obtained in the present measurement.

The γ-ray spectra, detected at 90° and 135° with respect to the beam direction, have been fitted simultaneously for the determination of each lifetime.
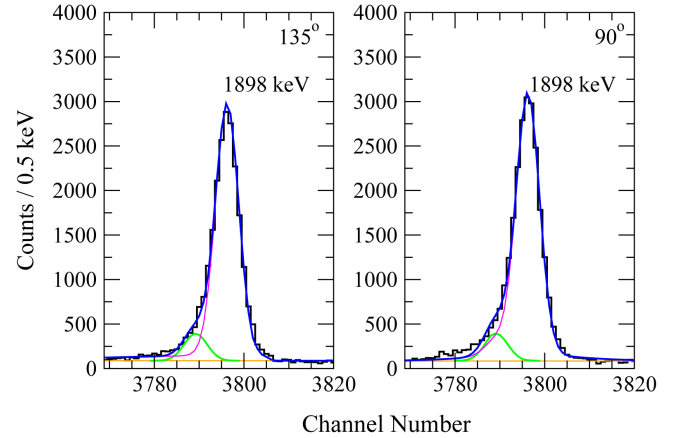

Fig. 4. (Color online) Experimental γ-ray energy spectra and fits to the Doppler shifted shapes for the 1898 keV ($13_1^+ \rightarrow 12_1^+$) transition. The spectra were produced by setting a narrow gate on the stopped component of the 726 keV transition decaying from the 12_1^+ state at 4717 keV excitation energy. The fitted total lineshape of the 1898 keV γ-ray transition is shown in blue. Shown is also the decomposition of the intrinsic lineshape into two gaussian peaks (magenta and green, respectively). See text for details. The resulting lifetime obtained in the present work $\tau_{13_1^+} = 1.36(17)$ ps is in agreement with the value previously obtained by Jungclaus et al. $\tau_{lit} = 1.26(17)$ ps [18].

As an example, for the determination of the lifetime of the 18^+ excited state, the lifetime value determined for the 19^+ excited state (3.08(69) ps) as well as the lifetime value of the 18^- excited state (5.04(34) ps) have been considered, giving a value of 0.55(7) ps in agreement with the
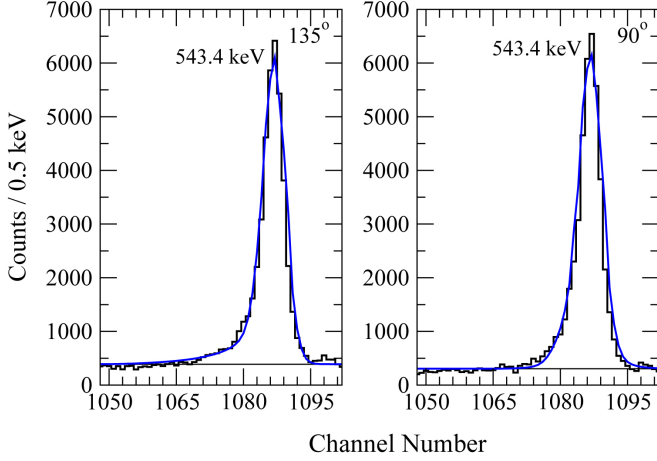
Fig. 5. (Color online) Lineshape fits for the 543.4 keV ($14_1^+ \rightarrow 13_1^+$) transition. The spectra are shown for events detected at 90° and 135° with respect to the beam direction (left and right panel, respectively) and obtained by gating on the 726 keV ($12_1^+ \rightarrow 10_1^+$) transition. The lifetime value of the 14_1^+ state obtained in the present work, 0.43(6) ps, is in agreement with the previously obtained value (0.48(6) ps) reported by Jungclaus et al. [18].
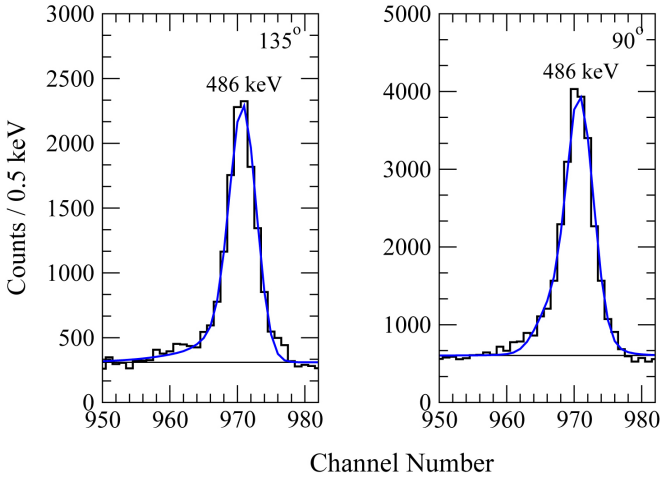

Fig. 7. (Color online) Fits to the observed lineshapes of the 394.5 keV ($19_1^+ \rightarrow 18_1^+$) γ-ray transition. The spectra are shown for events detected at 90° and 135° with respect to the beam direction (left and right panel, respectively) and obtained by gating on the 630 keV ($17_1^+ \rightarrow 16_1^+$) transition. The lifetime value of the 19_1^+ state obtained in the present work (3.08(69) ps) is within the previuosly reported upper limit (< 4.9 ps) [18].

Fig. 6. (Color online) Fits to the observed lineshapes of the 486 keV ($18_1^+ \rightarrow 17_1^+$) γ-ray transition. The spectra are shown for events detected at 90° and 135° with respect to the beam direction (left and right panel, respectively) and obtained by gating on the 630 keV ($17_1^+ \rightarrow 16_1^+$) transition. The resulting lifetime obtained in the present work ($\tau_{18_1^+} = 0.55(7)$ ps) is in agreement with the previously reported value ($\tau_{lit} = 0.52(3)$ ps) by Jungclaus et al. [18].

Fig. 8. (Color online) Fits to the observed lineshapes of the 1113.5 keV ($20_1^- \rightarrow 18_1^-$) γ-ray transition. The spectra are shown for events detected at 90° and 135° with respect to the beam direction (left and right panel, respectively) and obtained by gating on the 496 keV ($16_1^- \rightarrow 15_1^-$) transition. The lifetime value of the 20_1^- state obtained in the present work (2.20(31) ps) is within the upper limit (< 2.6 ps) reported by Jungclaus et al.[18].

value 0.52(3) ps given in Ref [18]. This value has been used as input, together with the lifetime value determined for the 19^+ excited state, for the determination of the lifetime of the 17^+ excited state, giving a value of 0.86(13) ps. The results of the lifetime analysis are summarized in Table 2. The statistical uncertainties are quoted, and typically around 10%. Additional, "systematic" uncertainties can be expected primarily from the empirical stopping power values employed. By changing between different stopping
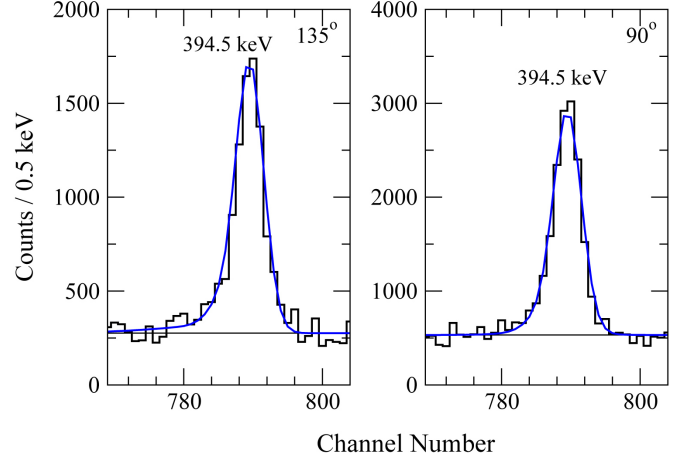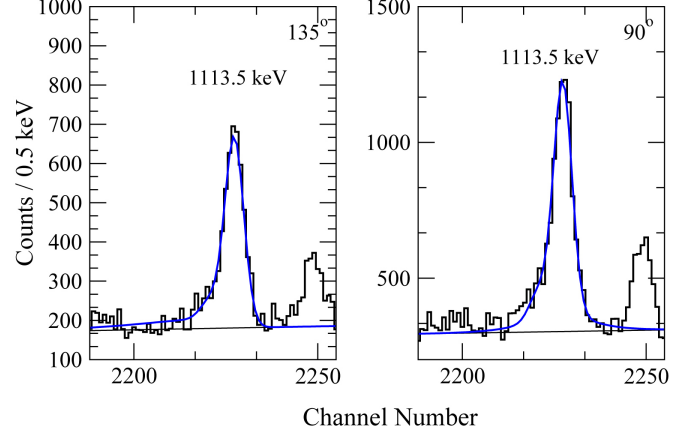
power tables (Ziegler at al. [13,14] and Northcliffe and Schilling [21], respectively) in the analysis, keeping other fitting conditions the same, such potential systematic uncertainties were investigated. The resulting variation in the final lifetime results were within 10%, and a mean variation considerably less was found. Furthermore, we found no systematic trend in these variations with respect to the stopping power model used, suggesting that these variations might mainly be of a different, perhaps numerical, nature. Hence, we believe that systematic uncertainties due to the employed stopping power model can conserva-

tively be set at 10%. Lifetime values and limits determined in Ref. [18] are also included in Table 2 for comparison. The lifetimes for the 13^+ state at 6614 keV, the 14^+ state at 7157 keV, and the 18^+ state at 9526 keV as well as upper limits on the lifetimes of the 15^+ state at 7773 keV, the 16^+ state at 8411 keV, the 17^+ state at 9041 keV, the 19^+ state at 9921 keV and the 20^- state at 11041 keV were previously reported [18]. The lifetimes of the latter five states have been determined for the first time in the present work.

4 Discussion

The structure of ^{94}Ru has been interpreted as two main even- and odd-parity groups of states built primarily on proton single-particle structures from the $g_{9/2}$ and $p_{1/2}$ subshells [18, 19, 22]. The spin-parity assignments for some of the strongest populated states that we have deduced from linear polarization and angular correlation measurements [20], confirm unambiguously this picture. The yrast and near-yrast states with spin $I \leq 12$ (including the 12_1^+ state) in the positive-parity structure and spin $I \leq 13$ (including the 13_1^- state) in the negative-parity structure are hence dominated by the $\pi(g_{9/2}^{-6})$ and $\pi(p_{1/2}^{-1}g_{9/2}^{-5})$ configurations, respectively. The agreement between calculated and experimental level energies for these states is typically quite good, while for states above 6 MeV excitation energy it is less perfect.

Several calculations using different shell model configuration spaces have been performed [4, 18, 19, 23, 24] in order to interpret the structure of high-lying states above $I \geq 13\hbar$ of ^{94}Ru, where core-excited configurations are expected to become important. However, this introduces formidable calculational challenges due to the large dimension of the model space and different truncation schemes are imposed by the limitations of current computational capabilities. The calculations presented in Ref. [23] were done in the model space $1p_{1/2}0g_{9/2}$, including also an excitation of one neutron or proton to the $1d_{5/2}$ shell, and it was found that the neutron core excitations $\nu(d_{5/2}g_{9/2}^{-1})$ play an important role. This is supported by the more recent calculations presented in Refs. [18] and [4]. In Ref. [20], we reported results of large-scale shell-model calculations in different model spaces in order to address the structure of this semi-magic nucleus. In particular using the $\pi(1p_{1/2}, p_{3/2}, f_{5/2}, g_{9/2})$ (denoted as fpg) model space relative to the $^{100}_{50}$Sn$_{50}$ core and in a further expanded model space including one-proton or one-neutron (core) excitations to the orbitals $g_{7/2}$ and $d_{5/2}$ (denoted as fpgd). We assumed isospin symmetry in the Hamiltonian and treated proton and neutron excitations on the same footing. We did not consider the continuum effect in proton orbitals above the $Z = 50$ shell closure which are not expected to be important here. A number of moderate- and high-spin states were suggested to be associated with a one-neutron core excitation from the $g_{9/2}$ to the $d_{5/2}$ subshell, which is consistent with earlier studies in, e.g., Ref. [19].

The M1 transition offers a special opportunity to test the many-body wave function and cross orbital excitations. In particular in relation to the fact that the magnetic dipole operator only links single-particle orbitals with the same orbital angular momentum [25], i.e. spin-orbit partners or states within the same single-j subshell. As a result, in the particular case of ^{94}Ru, the M1 transition properties can be expected to be dominated by coupling within the $g_{9/2}$ subshell and the possible excitation of nucleons from $g_{9/2}$ to its $g_{7/2}$ spin-orbit partner across the $N = 50$ shell gap, taking into account the significantly larger g-factor for states involving these orbitals compared with those of $p_{1/2}$ or $p_{3/2}$.

In the present work, we have performed shell model calculations for the M1 transitions in ^{94}Ru in the fpgd model space with the same Hamiltonian as described in Ref. [20]. We have calculated the lowest three eigenstates for each spin and parity and evaluated the reduced transition strengths for all possible M1 (and E2) transitions. For the calculations of $B(M1)$ reduced transition strengths, we used both the bare and the effective spin gyromagnetic factors with $g_s = 0.7 \cdot g_s(\text{free})$ while effective electric charges $e_\pi = 1.5e$ and $e_\nu = 0.8e$ were used for protons and neutrons, respectively, to calculate the E2 transition probabilities. This set of effective charges reproduces rather well the E2 transition properties of neighboring nuclei, both "below" and "above" the ^{100}Sn core. Fig. 9 shows the resulting calculated $B(M1)$ and $B(E2)$ values together with those reported by Jungclaus et al. [18] as "SM2", which were deduced from the work of Johnstone and Skouras [4], in comparison with the experimental values deduced in the present work.

While the yrast 12^+ state is dominated by the coupling within the $g_{9/2}$ subshell in our shell model calculations, the first 13^+ state is predicted to be the lowest-lying neutron core-excited state. The observed M1 transition between these two states is strongly hindered. The calculation reproduces reasonably well the observed hindrance, hence also confirming that the lowest core-excited configuration is based on the $\nu g_{9/2}$ orbital. The transition between the yrast 14^+ and 13^+ states and most other yrast M1 transitions are also relatively well reproduced by the calculations. The two magnetic transitions for which we find the most significant difference between theory and the experimental findings are those corresponding to $19_1^+ \rightarrow 18_1^+$ and $15_1^+ \rightarrow 14_1^+$. We also notice that the shell model calculation overestimates the excitation energy of the 19_1^+ state by nearly 600 keV. The discrepancies between experiment and theory concerning the energy of and transitions from this state might be due to the possible admixture from states involving two-neutron excitations at such high energy and possibly also proton excitations. On the other hand, it should also be mentioned that the predicted transition strength between the 19_1^+ and 18_2^+ states is quite large with $B(M1) = 2.5\mu_N$. We found that even a small mixture between the lowest two calculated 18^+ states will lead to enhanced M1 transition strength and better agreement with experiment. One may have a similar problem with the predictions for the 14^+ states. No

Table 2. Lifetimes of excited states in ^{94}Ru from the present work in comparison with previously reported values and limits. The excitation energy, spin-parity assignments and γ-ray energies are given in the first, second, and third column, respectively. Lifetimes, τ, determined using DSAM in the present work are given in column 4 while the lifetime results from Ref. [18] are given in column 5. Uncertainties (statistical) are given within parenthesis. Relative systematic uncertainties due to the modeling of stopping powers are estimated to be approximately 10% or less.

		Positive Parity		
E_x (keV)	$I_i^\pi \rightarrow I_f^\pi$	E_γ (keV)	τ (ps)	τ_{lit} (ps)
6614	$13_1^+ \rightarrow 12_1^+$	1898.2	1.36(17)	1.26(17)
7157	$14_1^+ \rightarrow 13_1^+$	543.4	0.43(6)	0.48(6)
7773	$15_1^+ \rightarrow 14_1^+$	615.6	0.32(4)	< 0.4
8411	$16_1^+ \rightarrow 15_1^+$	638.5	0.65(10)	< 1.0
9041	$17_1^+ \rightarrow 16_1^+$	630.1	0.86(13)	< 2.0
9526	$18_1^+ \rightarrow 17_1^+$	486.0	0.55(7)	0.52(3)
9921	$19_1^+ \rightarrow 18_1^+$	394.5	3.08(69)	< 4.9
		Negative Parity		
E_x (keV)	$I_i^\pi \rightarrow I_f^\pi$	E_γ (keV)	τ (ps)	τ_{lit} (ps)
11041	$20_1^- \rightarrow 18_1^-$	1113.5	2.20(31)	< 2.6

Table 3. The experimental transition probabilities B(M1) and B(E2) values which were deduced from the present measurements are given in columns 6 and 7, respectively. Uncertainties (statistical) are given within parenthesis.

		Positive Parity				
E_x (keV)	I_i^π	E_γ (keV)	I_f^π	σL	B(M1↓) $(\mu_N{}^2)$	B(E2↓) $(e^2\text{fm}^4)$
6614	13_1^+	1898.2	12_1^+	M1	0.0061(7)	
7157	14_1^+	543.4	13_1^+	M1	0.82(11)	
7773	15_1^+	615.6	14_1^+	M1	0.64(10)	
		1159.0	13_1^+	E2		178(22)
8411	16_1^+	638.5	15_1^+	M1	0.23(4)	
		1254.0	14_1^+	E2		34(5)
9041	17_1^+	630.1	16_1^+	M1	0.24(4)	
		1269.0	15_1^+	E2		31(5)
9526	18_1^+	486.0	17_1^+	M1	0.89(11)	
9921	19_1^+	394.5	18_1^+	M1	0.24(5)	
		880	17_1^+	E2		99(22)
		Negative Parity				
E_x (keV)	I_i^π	E_γ (keV)	I_f^π	σL	B(M1↓) $(\mu_N{}^2)$	B(E2↓) $(e^2\text{fm}^4)$
11041	20_1^-	597.5	19_1^-	M1	0.028(4)	
		1113.5	18_1^-	E2		166(23)

strong transition between the calculated lowest three 15^+ states and the yrast 14^+ state is expected, even though the first two 15^+ states lie very close to each other. On the other hand, a strong M1 transition is expected between the 15_1^+ and 14_2^+ states whereas the transition between the 14_2^+ and 13_1^+ states tends to vanish in the calculation. The agreement between theory and experiment would be significantly better for both $B(M1, 15_1^+ \rightarrow 14_1^+)$ and $B(M1, 14_1^+ \rightarrow 13_1^+)$ if one assumes that the observed 14_1^+ state is actually a mixture between the first two calculated 14^+ states.

In Ref. [18] shell-model calculations were reported with different effective interactions in two limited model spaces: one in the $p_{1/2}g_{9/2,7/2}d_{5/2,3/2}s_{1/2}$ space by allowing single-particle excitations across the $N = Z = 50$ shell closure (see values labeled as "SM2" in Fig. 9) and the other one in an extended model space consisting of protons in

$f_{5/2}p_{3/2,1/2}g_{9/2}$ and neutrons in $g_{9/2}d_{5/2}$ and referred to as "SM3" in Ref. [18]. Both calculations agree with the shell-model calculation performed in the present work concerning the dominance of $\nu g_{9/2} \rightarrow d_{5/2}$ cross-shell excitation in the structure of the high-lying states above 13^+. However, the SM2 and SM3 calculations presented in Ref. [18] give quite different results for the M1 transitions $19_1^+ \rightarrow 18_1^+$ and $15_1^+ \rightarrow 14_1^+$. The SM2 calculation performed in the more limited space reproduces rather well these transitions while the calculated B(M1) values are significantly reduced when the calculations are extended to include the $f_{5/2}$ and $p_{3/2}$ orbitals (SM3). In addition, the calculated spectrum shows worse agreement with experiment (c.f., Fig. 8 in Ref. [18]) in the latter case. These findings indicate that the contributions from the $p_{3/2}$ orbital to the M1 transitions may not have been properly described in the extended calculation, However, it is note-
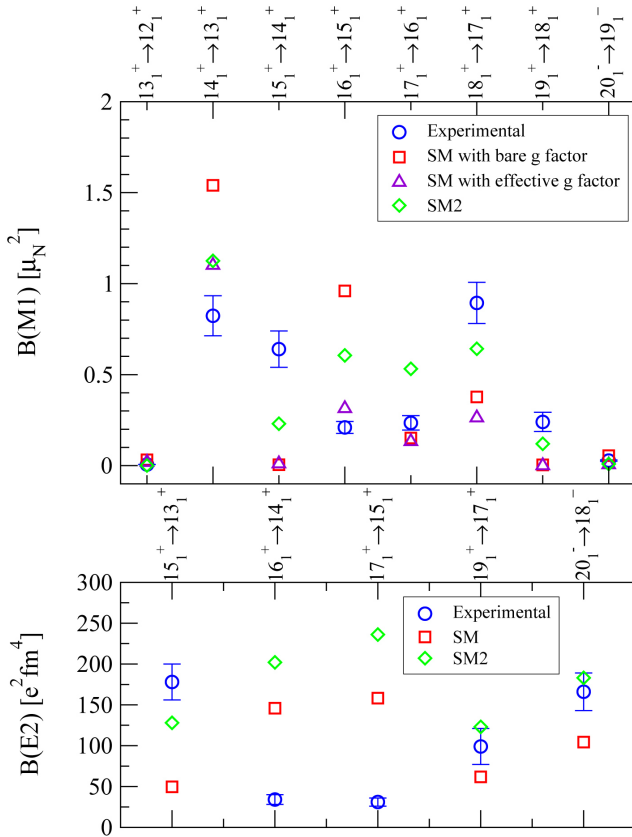
Fig. 9. (Color online) Comparison between B(M1) and B(E2) transition strengths and predictions by large-scale shell model calculations (this work and those reported by Jungclaus *et al.* [18] ("SM2") which were deduced from the work of Johnstone and Skouras [4]) for ^{94}Ru.

In the lower panel of Fig. 9 the B(E2) values deduced in this work are compared with both our shell-model calculations and those by Johnstone and Skouras [4], see Ref. [18]. Both calculations significantly overestimate the strengths for the transitions $16_1^+ \rightarrow 14_1^+$ and $17_1^+ \rightarrow 15_1^+$. All those states are calculated to be dominated by the $\nu g_{9/2} \rightarrow d_{5/2}$ cross-shell excitation. Again, this result seems to indicate that the observed 14_1^+ state corresponds to a mixture of the first two calculated 14^+ states. Similar admixtures may also be present for the observed 15_1^+ state.

Although we do not observe excited states with $I > 20\hbar$ in the present experiment due to the low excitation energy, it is clear that the yrast 20^- state has a special character, as can be seen from the level scheme of ^{94}Ru deduced in Ref. [19]. This state, which is predicted to be dominated by the maximally spin-aligned state of the $\pi(p_{1/2}^{-1}g_{9/2}^{-5}) \otimes \nu(d_{5/2}g_{9/2}^{-1})$ configuration (with more than 90% of the wave function) [19], lies more than 1 MeV lower in energy (2 MeV in the shell-model calculation) than the next $I = 20\hbar$ state and receives virtually all of the intensity flowing from the higher-lying states via multiple transitions of energies of around 2-4 MeV. Hence, the higher-lying negative-parity states are most likely built from configurations involving proton excitation from $p_{3/2}$ (and $f_{5/2}$) to $p_{1/2}$ or even a second neutron excitation across the $N = 50$ shell gap. The favored nature of this state and neighboring high-spin states is enhanced by the strong isoscalar $\pi g_{9/2}^{-1} \otimes \nu g_{9/2}^{-1}$ interaction in its spin-aligned coupling (see Refs. [1,2] and Refs. therein). The lifetime deduced for the yrast 20^- state in this work confirms its character, as well as that of the 19^- and 18^- states as belonging to the same $\pi(p_{1/2}^{-1}g_{9/2}^{-5}) \otimes \nu(d_{5/2}g_{9/2}^{-1})$ multiplet. It is noteworthy that Jungclaus *et al.* used significantly larger effective charges; $e_\pi = 1.77e$ and $e_\nu = 1.44e$, and achieve a better agreement with the data for the $20_1^- \rightarrow 18_1^-$ transition. Again, one may notice that there is a large difference between calculations in the two different model spaces. Hence, it seems that some of its observed strength is not accounted for by the calculations.

5 Summary

worthy that the SM2 and SM3 calculations presented in Ref. [18] were performed using different interactions. In order to clarify the contributions from different configurations to this effect, we have redone our calculations in the same model space by excluding the excitations of protons and neutrons out of the $f_{5/2}$ and $p_{3/2}$ orbitals. No significant changes in the calculated B(M1) values are seen. On the other hand, as mentioned above, one expects two 18^+ (and 19^+) states close to each other that are dominated by the configuration $\nu(d_{5/2}g_{9/2}^{-1}) \otimes \pi(g_{9/2}^{-6})$ and $\nu(d_{5/2}g_{9/2}^{-1}) \otimes \pi(p_{1/2}^{-2}g_{9/2}^{-4})$, respectively. Moreover, the transition between the calculated 19_1^+ and 18_2^+ state is very strong wheras the $19_1^+ \rightarrow 18_1^+$ transition is nearly cancelled. If the gap between the $p_{1/2}$ and $g_{9/2}$ orbitals is slightly reduced, around 600 keV, there will be a strong mixture between the configurations $\nu(d_{5/2}g_{9/2}^{-1}) \otimes \pi(g_{9/2}^{-6})$ and $\nu(d_{5/2}g_{9/2}^{-1}) \otimes \pi(p_{1/2}^{-2}g_{9/2}^{-4})$ with nearly equal contributions, leading to a B(M1) value that would agree quite well with the experimental findings. The calculated 19^+ states are not significantly influenced by this modification. We thus suggest that the $19^+ \rightarrow 18^+$ M1 transition is sensitive to the particle/hole nature of the proton $g_{9/2}$ configuration.

Lifetimes of high-spin states in the semi-magic $^{94}_{44}$Ru$_{50}$ nucleus have been measured using the DSAM technique, carried out with a thick metallic ^{58}Ni target. Lifetimes for the 15^+, 16^+, 17^+, 19^+ and 20^- states have been determined for the first time. The B(M1) and B(E2) strengths deduced from these measurements have been compared with large-scale shell-model calculations, confirming the importance of neutron cross-shell excitations in the high-spin structure of ^{94}Ru. The results highlight significant differences between calculations using different model spaces and interactions and indicate that further theory development is needed in order to properly describe the structure of nuclei in the vicinity of ^{100}Sn.

6 Acknowledgements

References

1. B. Cederwall et al., Nature **68**, (2011) 469.
2. C. Qi, J. Blomqvist, T. Bäck, B. Cederwall, A. Johnson, R. J. Liotta, and R. Wyss, Phys. Rev. C **84**, (2011) 021301.
3. M. Honma, T. Otsuka, T. Mizusaki, and, M. Hjorth-Jensen, Phys. Rev. C **80**, (2009) 064323.
4. I. P. Johnstone and L. D. Skouras, Phys. Rev. C **55**, (1997) 1227.
5. J. Simpson et al., Acta Phys. Hung. New Ser: Heavy Ion Phys. **11**, (2000) 59.
6. J. N. Scheurer et al., Nucl. Instrum. Methods Phys. Res. Sect. A **385**, (1997) 501.
7. J. Gál et al., Nucl. Instr. Meth. A **516**, (2004) 502.
8. O. Skeppstedt et al., Nucl. Instr. Meth. A **421**, (1999) 531.
9. D. Radford, Nucl. Instr. Meth. A **361**, (1995) 297.
10. F. Brandolini and R. V. Ribas, Nucl. Instr. Meth. A **417**, (1998) 150.
11. A. Gavron et al., Phys. Rev. C **21**, (1980) 230.
12. D. Bourgin et al., Phys. Rev. C **90**, (2014) 044610.
13. www.srim.org.
14. J. F. Ziegler, J. P. Biersack and U. Littmark, *The Stopping and Range of Ions in Matter* (Pergamon, New York 1985)
15. C. Wells and N. Johnson, ORNL Report **6689**, (1991) 44.
16. R. Bhattacharjee et al., Phys. Rev. C **90**, (2014) 044319.
17. A. Ertoprak, B. Cederwall et al., Acta Phys. Pol. **B48**, (2017) 325.
18. A. Jungclaus, D. Kast, K. P. Lieb, C. Teich, M. Weiszflog et al., Phys. Rev. C **60**, (2014) 014309.
19. H. A. Roth et al., Phys. Rev. C **50**, (1994) 1330.
20. F. G. Moradi, C. Qi and B. Cederwall et al., Phys. Rev. C **89**, (2014) 014301.
21. L. S. Northcliffe and R. F. Schilling, Atomic Data and Nuclear Data Tables **7**, (1970) 233.
22. A. Jungclaus et al., Eur. Phys. J. A **6**, (1999) 29.
23. K. Muto et al., Phys. Letters B **135**, (1984) 349.
24. M. Palacz et al., Phys. Rev. C **86**, (2012) 014318.
25. A. Bohr and B. Mottelson *Nuclear Structure* (World Scientific Publishing Co., Singapore 1998)